Retrospective Transmit Beamforming and Coherent Plane-Wave Compounding for Microvascular Doppler Imaging: A Comparison Study

Cristiana Golfetto, Ingvild Kinn Ekroll, *Member, IEEE*, Hans Torp, *Member, IEEE*, Lasse Løvstakken, *Member, IEEE*, and Jørgen Avdal, *Member, IEEE*

***Abstract*— Imaging blood flow in small vessels is of great clinical value for evaluating increased vascularization, potentially related to angiogenesis in cancer or inflammation processes in musculoskeletal disease. Using a traditional duplex imaging approach, a major challenge in color Doppler imaging is the limited amount of samples available for clutter filtering. Coherent plane-wave compounding (CPWC) enables a continuous high frame rate acquisition and improved image quality due to dynamic transmit focusing. However, the presence of moving scatterers in the image can lead to a loss in signal-to-noise ratio (SNR) and contrast. In this study, typical CPWC sequences for low-flow imaging were compared with retrospective transmit beamforming (RTB) sequences with similar frame rates and transmit power. The comparison was based on resolution, contrast, and SNR, using a stationary phantom, a flow phantom, a thread phantom, and *in vivo* recordings of blood vessels in the thyroid and kidney. A model was developed to estimate the difference in SNR between RTB and CPWC in the presence of static and moving scatterers while varying the transmit sequence parameters. The model predicted that RTB may yield an increased SNR compared with CPWC, especially for flow imaging, where the SNR difference reached 6 dB for a maximum velocity of 15 cm/s. The measured SNR values were in agreement with the predicted values, both in the case of stationary scatterers and for the flow phantom. We further demonstrated that reducing beam density to increase frame rate is associated with spatial undersampling (stripe) artifacts for RTB and grating lobes for CPWC. Both phantom and *in vivo* results indicate that transmit focusing may be beneficial in a low-flow imaging setup that, combined with adaptive clutter filtering, can yield superior microvascular imaging.**

***Index Terms*— Coherent plane-wave compounding (CPWC), microvascular Doppler imaging, retrospective transmit beamforming (RTB), synthetic transmit focusing.**

Manuscript received July 8, 2020; accepted October 20, 2020. Date of publication October 26, 2020; date of current version March 26, 2021. *(Corresponding author: Cristiana Golfetto.)*

Cristiana Golfetto, Hans Torp, Lasse Løvstakken, and Jørgen Avdal are with the Centre for Innovative Ultrasound Solutions (CIUS), Norwegian University of Science and Technology (NTNU), 7491 Trondheim, Norway, and also with the Department of Circulation and Medical Imaging, Norwegian University of Science and Technology (NTNU), 7030 Trondheim, Norway (e-mail: cristiana.golfetto@ntnu.no).

Ingvild Kinn Ekroll is with the Centre for Innovative Ultrasound Solutions (CIUS), Norwegian University of Science and Technology (NTNU), 7491 Trondheim, Norway, also with the Department of Circulation and Medical Imaging, Norwegian University of Science and Technology (NTNU), 7030 Trondheim, Norway, and also with Kirurgisk Klinikk, St. Olavs Hospital HF, 7030 Trondheim, Norway.

This article has supplementary downloadable material available at http://ieeexplore.ieee.org, provided by the authors.

Digital Object Identifier 10.1109/TUFFC.2020.3033719

I. Introduction

ULTRASOUND color Doppler imaging of small vessels (<1 mm) is often desired, for instance, in clinical scenarios where abnormal growth of vessel structures develop, such as angiogenesis in cancer [1], or due to inflammation processes in musculoskeletal disease [2]. Current clinical systems offer dedicated imaging setups for this application, traditionally based on line-by-line focused imaging, where a low pulse repetition frequency (0.25–1 kHz) is used to increase sensitivity to the lower flow velocities. A packet-based color Doppler acquisition is then typically combined with B-mode in a duplex modality, and a power Doppler display is often preferred. Even for high-end systems with parallel beamforming capabilities, this approach yields low frame rates (<10 Hz) and with a detection capability substantially limited by the available packet size (<20) due to clutter filtering constraints.

Clutter filtering is a major challenge for low-flow imaging using the traditional imaging setup since only 10–20 temporal samples are available for processing. For traditional high-pass filters, a wide filter transition region can lead to substantial attenuation of signals from low blood velocities or induce severe clutter signal leakage, visible as flashing artifacts in the images.

Recently, coherent plane-wave compounding (CPWC) has been introduced [3]. By emitting unfocused pulses covering the full aperture and exploiting software beamforming, ultrahigh frame rates can be reached (>10 kHz). It has been shown that coherently compounding beamformed signals from a sufficient number of plane waves transmitted with different steering angles results in an effective lateral beam profile, which approximates that of a focused beam at all depths. CPWC can offer a duplex modality with good B-mode quality

and continuous acquisition for Doppler processing on linear arrays. For low-flow and small-vessel imaging, this has several advantages: high frame rates and a wide region of interest, dynamic transmit focusing for improved contrast and signal-to-noise ratio (SNR) throughout the image region, and a continuous acquisition that provides new opportunities for clutter filtering and low-flow detection. Higher order finite impulse response (FIR) or infinite impulse response (IIR) filters with steep transition regions can be used to improve detection. Furthermore, adaptive clutter filtering can then provide substantially improved clutter rejection even for accelerated tissue movement. Eigendecomposition-based clutter filters [4]–[6] have proven highly efficient in low-flow imaging applications [7]–[9]. For other applications, adaptive FIR filters may yield similar results [10], [11].

Although the approach is successfully used in several applications, including functional ultrasound (fUS) imaging of the brain [12], [13], there may still be room for improvement. Dynamic transmit focusing is based on the coherent combination of several transmit pulses. For valid reconstruction, this process assumes that the target is stationary, which blood flow inherently is not. It has previously been shown that unless motion compensation is introduced, the motion of blood can lead to a substantial loss in SNR [14]. While motion compensation is possible, it is computationally demanding and can also fail.

In this work, we investigate the alternative of using focused pulses, combined with coherent compounding of the beamformed signals from neighboring beams. This is often referred to as virtual source imaging or retrospective transmit beamforming (RTB) [15]. Instead of reconstructing the lateral bandwidth through several angled plane waves, traditional scanning is used by moving the transmitting aperture across the array. Observed from a fixed image point, dynamic transmit focusing is achieved as successive transmissions fill in different lateral components in the Fourier domain. The approach is dependent on sufficient lateral sampling on transmit to avoid image artifacts, but a high frame rate (e.g., 250–500 frames/s) for low-flow imaging can still be achieved for shallow depths. Potential advantages of this approach are: 1) that careful placement of the image focus can lead to high contrast and SNR when combining fewer transmits, important for avoiding motion artifacts and 2) that we avoid the excitation of the full aperture for each emission, which is beneficial for limiting probe heating and for reducing the amount of energy leaking out of the spatial region of interest.

We describe the two acquisition techniques in the setting of low-flow imaging. The aim of this study is to investigate whether the use of RTB may be beneficial in this application and study the advantages and disadvantages of each acquisition technique. The two sequences are implemented on a clinical scanner, and their performance is evaluated in terms of resolution, contrast, and SNR. A stationary phantom, a flow phantom, and a thread phantom are used for the comparison. In addition, a model is developed to estimate the SNR difference between RTB and CPWC techniques using static and moving scatterers. *In vivo* recordings of blood vessels in the thyroid and kidney are used to evaluate the feasibility of the designed setups for Doppler imaging.

This article is structured as follows. Section II describes CPWC, RTB, and the model to estimate the SNR difference. The specific acquisition setups are given in Section III, which also describes how resolution, contrast, and SNR are measured. Results are presented in Section IV and discussed in Section V.

II. Background

A. Coherent Plane-Wave Compounding

A CPWC sequence is made of N consecutive emissions of broad beams with different steering angles θ_n. All the transmit angles are symmetrically distributed around 0° and equally spaced [14], as illustrated in Fig. 1. An insonification with a single plane wave yields an image with low resolution and contrast. Coherent summation of several such low-resolution images is, therefore, used to obtain images with synthetic transmit focusing, increasing image resolution and contrast.

The resolution of a CPWC image can be quantified by analyzing the spatial Fourier transform of the transmitted fields, i.e., the point spread function (PSF) in the spatial frequency domain (k-space). When coherently compounding plane waves, the contribution from each angle results in a range of spatial frequencies surrounding a k-space line. The steering angle determines the orientation of the k-space line. Covering a larger range of angles will, therefore, improve lateral resolution. The transmit F-number ($F_{\#\mathrm{tx}}$) is then solely determined by the maximum steering angle [16]

$$F_{\#\mathrm{tx}} = \frac{1}{2\tan(\alpha_{\max})} \approx \frac{1}{2\,\alpha_{\max}} \tag{1}$$

where $\alpha_{\max}$ is expressed in radians and the approximation is valid as long as $\alpha_{\max}$ is relatively small.

Contrast is defined as the ability to detect an anechoic object in a homogeneous scattering medium [3]. The presence of grating lobes, side lobes, and axial lobes leads to reduced contrast [17]. As (1) shows that lateral resolution is only dependent on the maximum angle and not on the angle sequence, the same resolution and higher frame rate could be achieved by decimating the angle sequence. However, this introduces grating lobes that increase with the decimation factor, resulting in lower contrast [16].

In [3], the contrast was measured and compared for three different imaging acquisitions: coherent compounding of 71 plane waves, conventional multifocus imaging with four focal depths, and optimal multifocus imaging. For standard multifocus imaging, the contrast reached its maximum at the focal depths and decreased rapidly outside the focal region. The CPWC sequence, however, yielded contrast values that were approximately constant for all depths. The study described in [3] also showed the compromise between the number of transmitted plane waves and the contrast of the image. Indeed, significant improvement was achieved by increasing the number of insonifications. Coherent compounding of images from 45 angles resulted in contrast comparable to that of conventional multifocus imaging at the focal depths.

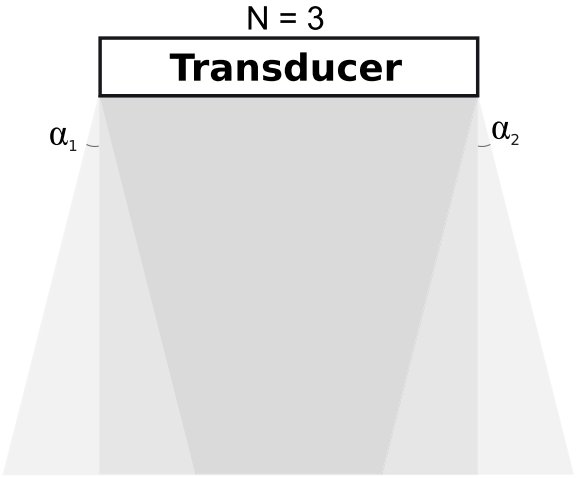

Fig. 1. Example of CPWC: three plane waves are transmitted and compounded. Angles α_1 and α_2 are equal and symmetrical around 0°. The least transparent region is the region with the highest resolution, contrast, and SNR. This region is determined by the aperture size and the angle span $\pm\alpha_{1,2}$.

The number of compounded plane waves also has an impact on SNR. When coherently compounding N images, signals from different emissions are added coherently in the focus, whereas the noise is added incoherently. This leads to an SNR gain of $\sqrt{N}$. In [3], it was indicated that compounding 71 plane waves yielded higher SNR than that of optimal multifocus imaging for all depths.

The presence of moving scatterers in the image may cause a loss of SNR/resolution, as described in [14] and [16]. If $\text{PRF}_{\max}$ denotes the firing rate, spatial shifts in the axial direction equal to $v = \text{PRF}_{\max}\lambda/4$ will lead to complete destructive interference between two transmissions and maximum degradation in SNR [18]. An SNR decrease of about 2 dB has been reported for velocities around the Nyquist limit [16], [18]. As SNR can be quite low when imaging blood flow, a 2-dB loss can result in strongly reduced image quality [14].

When applying CPWC, other issues can arise, such as axial lobes, as described in [17], [19], and [20]. Axial lobes appear below the main lobe and extend along the axial direction. In [3], it was shown experimentally that increasing the number of compounded plane waves leads to better contrast; however, axial lobes may yield a local reduction of contrast [17]. These artifacts arise because the assumption that plane waves have perfectly planar wavefronts is violated. Indeed, waves emitted by different elements of the transducer will not reach any given spatial point (x, z) simultaneously. Signals arriving successively will result in delayed echoes, which will be imaged at higher depths. Axial lobes may be reduced by using a probe with a smaller pitch or by applying angle-dependent transmit apodization (ADTA), as described in [20].

B. Retrospective Transmit Beamforming

RTB employs a conventional scan sequence using focused beams. Each beam partially overlaps with the preceding and/or following beam. Receive beamforming is performed similarly to CPWC, using expanding aperture and apodization. The overlapping regions between beams are coherently compounded according to a virtual source model [21], and the set of transmissions used to generate the image is determined individually for each pixel. When designing an RTB sequence, some parameters need to be defined, such as the aperture width, the interbeam distance, and the number of firings per frame. These parameters determine a tradeoff between SNR/contrast, image width, and frame rate. This technique has several potential advantages. Compared with conventional focused imaging, it yields increased contrast and SNR in the overlapping regions, whereas, compared with CPWC, not all the elements of the transducer are activated for each emission, improving the tradeoff between transmit voltage and probe heating.

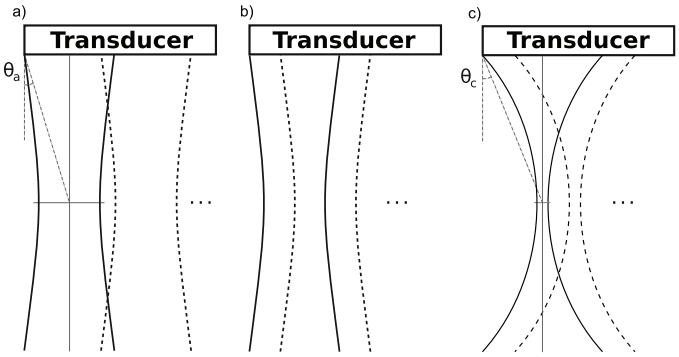

Fig. 2. Examples of RTB sequences. (a) Small aperture and large interbeam distance and large $F_{\#\text{tx}}$. (b) Small aperture and small interbeam distance and large $F_{\#\text{tx}}$. (c) Large aperture and small interbeam distance and small $F_{\#\text{tx}}$. Note that a small $F_{\#\text{tx}}$ corresponds to a large critical angle and $\theta_b = \theta_a < \theta_c$.

For both RTB and CPWC, coherent compounding leads to improved performance in terms of SNR, contrast, and resolution. For RTB, this improvement is achieved by compounding echoes from focused beams, rather than unfocused beams. Because focused beams are employed, a smaller spatial region is insonified for an RTB acquisition compared with CPWC. Fig. 2 illustrates different RTB acquisition setups, for which beamwidth and interbeam distance determine a tradeoff between resolution and frame rate.

Also for RTB, resolution may be quantified by studying the PSF in k-space. The opening angle, also called the critical angle, depends on the $F_{\#\text{tx}}$ of each focused transmission

$$\theta = \arctan\left(\frac{1}{2F_{\#\text{tx}}}\right). \tag{2}$$

The support of the PSF in k-space spans the range of angles between $-\theta$ and θ. Lowering $F_{\#\text{tx}}$ yields a larger region of support in k-space, which implies better lateral resolution. One way to achieve this is by increasing the aperture size while maintaining the focal depth, as illustrated in Fig. 2 (right). This, however, may require the use of a lower transmit voltage to avoid probe overheating. Another disadvantage of having a low $F_{\#\text{tx}}$ and, thus, high resolution is that more beams are required in order to avoid undersampling, which again leads to a lower frame rate.

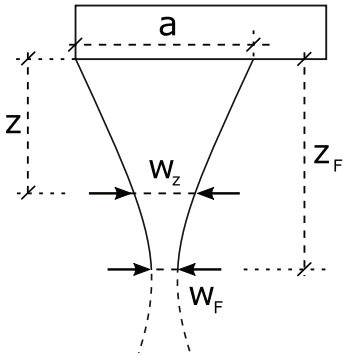

Fig. 3. Simplified sketch of a focused beam. The beamwidth at the depth z (w_z) can be calculated using linear interpolation.

The signal intensity using RTB can be estimated using certain approximations. One approximation is that the backscattered energy is inversely proportional to the beamwidth due to focusing. Another approximation is that the beamwidth decreases linearly from the aperture to the focal depth. As stated in Section II-A, the SNR after compounding is proportional to $\sqrt{N}$, where N is the number of overlapping beams. The beamwidth w_z at depth z can be calculated by linear interpolation using the following equation (see Fig. 3):

$$w_z = w_F \frac{z}{z_F} + a\frac{z_F - z}{z_F} \tag{3}$$

where z_F denotes the focal depth, a is the aperture, and w_F is the beamwidth at the focal depth given by

$$w_F = F_{\#tx}\lambda.$$

Once the beamwidth at a specific depth is known, the number of overlapping beams can be estimated as the beamwidth divided by the interbeam distance

$$N(z) = \frac{w_z}{n_{step}\, l} \tag{4}$$

where n_{step} is the number of elements between the beam centers and l is the pitch. Combining (3) and (4), $N(z)$ is equal to

$$N(z) = \frac{w_z}{n_{step}\, l} = \frac{1}{z_F}\frac{w_F\, z + a(z_F - z)}{n_{step}\, l} \tag{5}$$

and increases as the interbeam distance decreases.

C. Model to Estimate SNR Difference

In the following, a model is developed to obtain an estimate of the SNR difference between RTB and CPWC. Let $\mathbf{s}(k)$ denote the beamformed IQ signal at spatial point $(x_s,\ z_s)$ from transmission k, from a scatterer moving through positions $(\mathbf{x}(k), \mathbf{z}(k))$

$$\mathbf{s}(k) = \mathbf{w}(k)e^{j\mathbf{d}(k)}\ \mathbf{w}(k) = \mathbf{w}_{tx}(k)\mathbf{w}_{rx}(k)\mathbf{w}_{ax}(k) \tag{6}$$

in which $\mathbf{w}$ accounts for the position of the scatterer within the beam and $e^{j\mathbf{d}}$ is phase factor due to the axial motion. The weighting functions $\mathbf{w}_{tx}$ and $\mathbf{w}_{rx}$ account for the lateral position of the scatterer within the transmit and receive beams, and $\mathbf{w}_{ax}$ denotes the axial weighting function. The phase shift between transmissions is calculated considering that a spatial shift of $\lambda/2$ in axial direction corresponds to 2π radians. Given a scatterer moving with axial velocity v, the phase shift $\mathbf{d}(k)$ is equal to

$$\mathbf{d}(k) = \frac{4\pi k v}{\mathrm{PRF}\,\lambda}. \tag{7}$$

If the scatterer is stationary, $\mathbf{d}(k) = 0$ and $e^{j\mathbf{d}(k)} = 1$.

1) RTB$_{tx}$: For a focused beam, the lateral beam profile at the focal depth is approximated by a sinc function with the first zero at $F_{\#}\lambda$. For RTB acquisitions, multiple focused beams are compounded in order to regain signal power and resolution also outside the transmit focal depth. In this work, a sinc function is used to approximate the lateral beam profile also outside the focus, setting the first zero at the one-sided beamwidth w_z at depth $\mathbf{z}(k)$. The lateral position of the scatterer is given by the sum of the lateral displacement of the scatterer and the relative lateral displacement $\mathbf{r}(k)$ of the center of the active aperture

$$\mathbf{w}_{txr}(k) = \mathrm{sinc}\left(\frac{\mathbf{x}(k) - x_s + \mathbf{r}(k)}{w_z}\right). \tag{8}$$

If the scatterer is stationary, $\mathbf{x}(k) = x_s$, and the lateral position of the scatterer relative to the beam is solely determined by the movement of the scan.

2) CPWC$_{tx}$: In [3], it was shown that, when compounding plane waves, the lateral variation may be approximated by a sinc function. The beamwidth can be approximated by $F_{\#tx}\lambda$ at all depths. The transmit weighting function is then equal to

$$\mathbf{w}_{txc}(k) = \mathrm{sinc}\left(\frac{\mathbf{x}(k) - x_s}{F_{\#txc}\lambda}\right). \tag{9}$$

If $v = 0$, again, we get $\mathbf{x}(k) = x_s$ and $\mathbf{w}_{txc}(k) = 1$.

3) Receive Weighting: The CPWC and RTB sequences have the same $F_{\#rx}$, and dynamic focusing is applied on receive. Assuming that the receive beam is aligned with the scatterer position, $\mathbf{w}_{rxc}$ and $\mathbf{w}_{rxr}$ are equal to

$$\mathbf{w}_{rxc}(k) = \mathbf{w}_{rxr}(k) = \mathrm{sinc}\left(\frac{\mathbf{x}(k) - x_s}{F_{\#rx}\lambda}\right). \tag{10}$$

4) Axial Weighting: The axial weighting functions $\mathbf{w}_{axc}$ and $\mathbf{w}_{axr}$ are given by the envelope of the transmitted pulse $E(t_f)$

$$\mathbf{w}_{axc}(k) = \mathbf{w}_{axr}(k) = E\left(\frac{2(\mathbf{z}(k) - z_s)}{c}\right) \tag{11}$$

where t_f denotes fast time and the pulse is centered around $t_f = 0$. As the axial weighting function is a function of depth, it is dependent on the axial velocity of the scatterer. When $v = 0$, the axial weighting function is constant.

The power of the compounded signal is found by first calculating the contribution from a scatterer moving with velocity v, denoted as p_c and p_r for CPWC and RTB, respectively

$$p_c(v) = \frac{1}{w_c}\left|\sum_{k=1}^{N_c}\mathbf{s}_c(k)\right|^2, \quad p_r(v) = \frac{1}{w_z}\left|\sum_{k=1}^{N_r}\mathbf{s}_r(k)\right|^2 \tag{12}$$

where w_c denotes the aperture size for CPWC. The underlying assumption is that both acquisitions transmit the same power, distributed evenly throughout the insonated cross sections.

TABLE I
SEQUENCE DESIGNS FOR CPWC AND RTB

Firings \ $F_{\#tx}/\alpha_{max}$	$F_{\#tx}$= 1.4	α_{max} = 12°	α_{max} = 20°
48	RTB1	CPWC1	CPWC3
24	RTB2	CPWC2	CPWC4

TABLE II
ACQUISITION AND PROCESSING PARAMETERS FOR CPWC AND RTB

	CPWC	RTB
Central frequency [MHz]	8	8
Focal depth [cm]	//	4.07
N. elements activated	192	128
Inter-beam distance [nr. elements]	//	2/4
Pulse cycles	2	2
Pitch [mm]	0.229	0.229
Aperture size [cm]	4.40	2.93
Frame rate [Hz]	177/344	177/344
PRF [Hz]	8496	8496
Receive apodization	Boxcar	Boxcar
Packet size *in vitro*	200	200
Packet size *in vivo*	128	128
Vel. stop FIR [cm/s]	0.08	0.08
Vel. pass FIR [cm/s]	0.12	0.12
Stopband att. FIR [dB]	70	70

The ratio between the cross sections for RTB and CPWC is equal to the ratio between the corresponding beamwidths. In this work, we assume a uniform velocity distribution between 0 m/s and $v_{\max}$; in that case, the total power becomes equal to

$$P_c = \int_0^{v_{\max}} p_c(v)\,dv, \quad P_r = \int_0^{v_{\max}} p_r(v)\,dv. \tag{13}$$

The SNR difference between RTB and CPWC at a certain depth is the sum of two contributions: the total power of the scatterers and the noise floor that is proportional to the number of compounded beams

$$\begin{aligned} \mathrm{SNR_r} - \mathrm{SNR_c} &= 10\log_{10}\left(\frac{P_r}{N_r}\right) - 10\log_{10}\left(\frac{P_c}{N_c}\right) \\ &= 10\log_{10}\left(\frac{P_r}{P_c}\right) - 10\log_{10}\left(\frac{N_r}{N_c}\right). \end{aligned} \tag{14}$$

III. METHOD

A. Design of Acquisition Schemes

A locally modified commercial scanner (GE-Vingmed Vivid E95) equipped with a GE 9L-D linear probe was used for continuous acquisitions of the channel data. CPWC and RTB sequences were designed to have the same frame rate (number of firings) and output power to enable a fair comparison. Six sequence designs were investigated. Specifics can be found in Table I.

Table II illustrates the parameters for CPWC and RTB setups and further processing. Beamforming was performed offline using MATLAB (R2019a, Mathworks, USA).

B. Stationary Phantoms

A CIRS model 050 near-field ultrasound phantom was imaged using CPWC1 and RTB1 in order to compare lateral resolution and SNR. The resolution was measured using a single frame as −6-dB and the −12-dB lateral width of the beamformed data through three scatterers located at depths of 1, 1.9, and 2.8 cm.

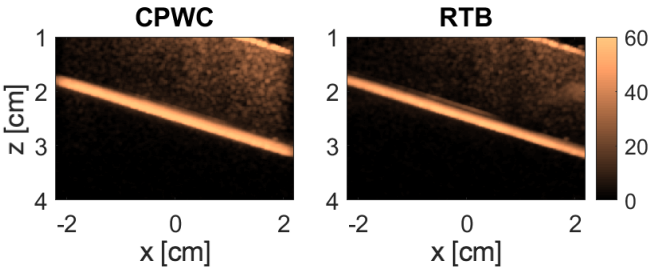

Fig. 4. Power Doppler images of the tube in the flow phantom after FIR filtering using the CPWC1 (left) and RTB1 (right) transmit sequences.

To estimate the SNR difference, (14) was used. A 5 × 5 averaging filter was applied to lower the variance of the signal power estimate, and separate recordings with the transducer in contact with only air were used to estimate the noise floor for both sequences. The SNR difference between RTB and CPWC images was calculated. The values for SNR difference midimage were then averaged along the lateral direction.

A circular anechoic cyst located at 1.5-cm depth was imaged using the different acquisition schemes in order to estimate contrast. The contrast was calculated as the ratio between the mean power inside the cyst and the mean power around the cyst. A circular region defining the cyst was manually selected, and the region around the cyst was limited by a rectangular region with dimensions 7 mm × 5 mm.

Recordings of the stationary phantom were also used to investigate the behavior of the RTB approach around the focal depth when reducing the number of firings from 48 to 24.

A phantom made of a thread immersed in water (JJ&A Instruments, Duvall, WA, USA) was used to compare the PSFs for the different acquisition schemes in Table I. In order to visualize the lateral profile of the PSF, a two-point moving average filter was applied to yield a smoother curve.

C. Flow Phantom

A micropump (Ismatec) was connected to a peripheral vascular Doppler flow phantom with tube diameter equal to 2 mm (see Fig. 4). PW Doppler was used prior to the flow phantom recordings to provide estimates of the velocity magnitude in the central part of the tube for different flow rates. These measurements were performed using a BTF angle of approximately 45°. Finally, RTB and CPWC recordings were performed using a range of flow rates corresponding to velocities between 2 and 15 cm/s, with BTF angle equal to 73°. Clutter filtering described in Section III-F was applied in order to suppress the clutter signal. A spatial averaging filter with kernel 6 × 6 samples was applied to lower the variance of the power estimator. CPWC1 and RTB1 power Doppler images were compared, and the SNR difference between RTB1 and CPWC1 was calculated from 213 points along the central axis of the tube, centered around a depth of 2.3 cm.

D. Predicted SNR Difference

The model described in Section II-C was used to estimate the SNR difference between RTB and CPWC. Assuming to be

located along the central axis of the transducer, the number of overlapping beams in CPWC, N_c, was set equal to the number of transmitted plane waves. In the case of moving scatterers, the predicted SNR difference at a given depth was calculated using (13) and (14), by summing the power contributions from 300 velocity components between 0.2 cm/s and the maximum measured velocity.

E. In Vivo Recordings

In vivo recordings were performed on the thyroid of two healthy volunteers and the kidney of a healthy volunteer. The recordings of the thyroid captured flow both in the common carotid artery and thyroid vessels. Holding the probe in the same position, two recordings were acquired using CPWC1 and RTB1 sequences, respectively. An observation window of 0.1 s was used for power Doppler images.

F. Clutter Filtering

1) FIR: In the flow phantom recordings, a 138th-order FIR filter was applied to remove the clutter signal. Table II illustrates the values for velocity cutoffs and stopband attenuation. The temporal observation window allowed averaging over 0.3 s after clutter filtering.

2) SVD: For *in vivo* recordings, an adaptive filter was applied to enable detection of the low-velocity flow in the small vessels. An observation window of 0.7 s was used for blood-clutter separation based on the spatial correlation between eigenvectors. A correlation map between spatial eigenvectors was used, denoted as a similarity matrix [22], and the clutter dimension was manually selected. Denoting this value as t, the subspace generated by the first t eigenvectors was removed. Given a matrix $\mathbf{A}$ with dimension (n_s, n_t) where n_s denotes the number of spatial points and n_t indicates the pulse transmissions, the filtered signal matrix $\mathbf{Y}$ is equal to

$$\mathbf{Y}^T = \left(\sum_{k=t+1}^{n_P} \sigma_k \mathbf{u}_k \mathbf{v}_k^H \right) \mathbf{A}^T \tag{15}$$

where σ_k are the singular values of $\mathbf{A}$, $\mathbf{u}_k$ are the spatial singular vectors, and $\mathbf{v}_k$ are the temporal singular vectors. The parameter n_p denotes the packet size.

IV. Results

A. Stationary Phantoms

Fig. 5 shows the scatterers in the stationary phantom imaged using CPWC1 and RTB1. The imaging depth is displayed in cm, where 1 cm $\approx$ 52 wavelengths. Fig. 6 displays the corresponding lateral beam profiles at three different depths. The beamwidth at 1 cm is smaller using CPWC. The two curves are more similar at 1.9 cm, especially close to the peak. At the highest depth, RTB yields a narrower beam. Table III illustrates the values for resolution using −6-dB and −12-dB lateral widths. These values increase with depth in both approaches. With the given setup, the resolution decreases more rapidly with depth using CPWC than RTB.

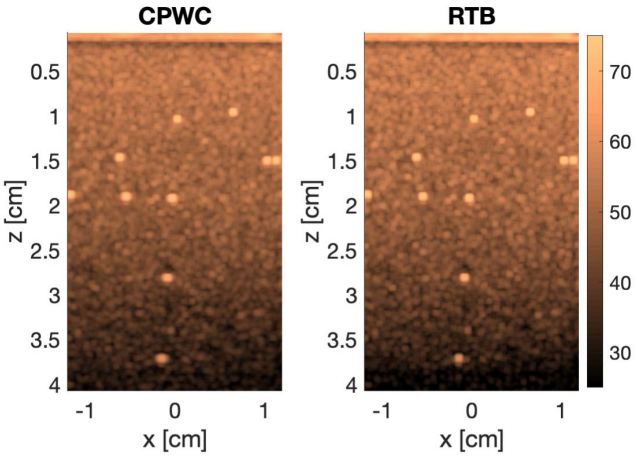

Fig. 5. Scatterers in the stationary phantom imaged using the CPWC1 (left) and RTB1 (right) transmit sequences.

TABLE III
RESOLUTION AT THREE DIFFERENT DEPTHS USING THE TWO METHODS. VALUES ARE EXPRESSED IN mm

	1 cm	1.9 cm	2.8 cm
CPWC1 -6 dB	0.33	0.40	0.50
RTB1 - 6 dB	0.39	0.43	0.45
CPWC1 -12 dB	0.44	0.63	0.80
RTB1 - 12 dB	0.54	0.58	0.64

TABLE IV
VALUES OF CONTRAST USING THE DIFFERENT ACQUISITION SCHEMES

	Contrast [dB]
RTB1	-24.1
RTB2	-22.1
CPWC1	-24.6
CPWC2	-24.4
CPWC3	-23.8
CPWC4	-22.8

In Fig. 7, the stationary phantom has been imaged with sequences RTB1 and RTB2. It can be observed that reducing the number of beams results in stronger stripe artifacts at the bottom of the image, in proximity to the focal depth.

Fig. 8 displays the circular anechoic cyst imaged using the different transmit sequences. The sequences using 48 firings have approximately the same contrast, which is approximately 1–2 dB higher than that of the sequences with 24 firings. Table IV illustrates the estimated values for contrast using the different acquisition sequences. The highest values are obtained with CPWC1, CPWC2, and RTB1, followed by CPWC3, whereas CPWC4 and RTB2 yield the lowest contrast.

Fig. 9 illustrates the PSF using the investigated transmit sequences. For both sequences, side lobes are visible, whereas, in the CPWC images, grating lobes also appear at the sides of the image. The artifacts become stronger when reducing the number of firings in the RTB sequence or when increasing the maximum steering angle in the CPWC case while maintaining the number of emissions. Fig. 10 shows the lateral extent of the PSF using RTB1, CPWC1, and CPWC3. The beam profiles using RTB1 and CPWC3 are very similar, whereas CPWC1 yields the highest beamwidth.

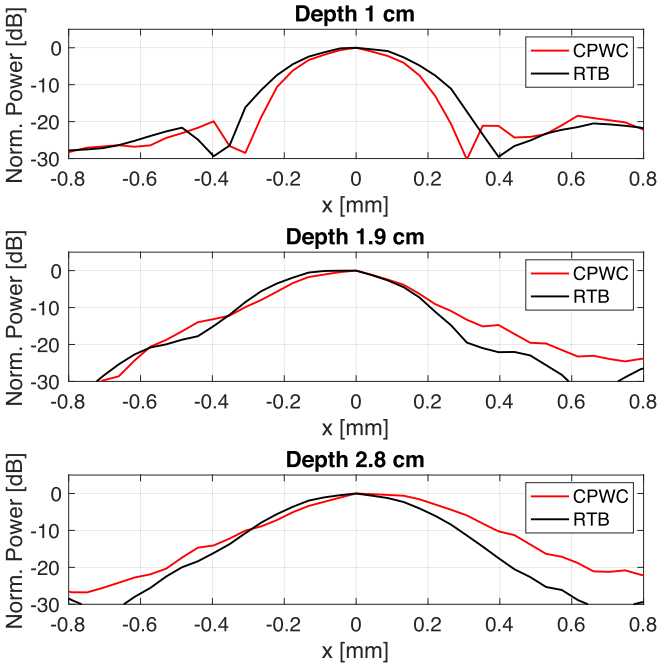

Fig. 6. Lateral beam profiles from the stationary phantom at three different depths. Beam profiles for the CPWC1 and RTB1 setups are displayed in red and black color, respectively.

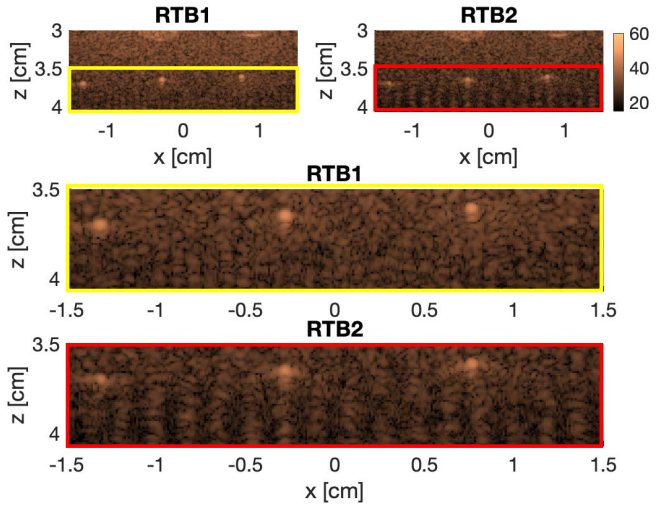

Fig. 7. Comparison between RTB1 and RTB2. The yellow and the red rectangle indicate the region around the focal depth where stripe artifacts become stronger when reducing the number of transmissions.

B. Predicted and Measured SNR Difference

Fig. 11 illustrates the SNR difference between the RTB1 and CPWC1 sequences using the stationary phantom. The power ratio varies laterally within the image, yielding higher values close to the edges. By studying the SNR difference at the point scatterers, we can observe that resolution in RTB1 is higher, which supports the findings in Fig. 6 and Table III.

Fig. 12 shows the SNR difference for the investigated sequences as a function of depth, as predicted by the signal model and measured in the stationary phantom. As may be observed, the measured values correspond well with the predicted values, with RTB yielding a higher SNR than CPWC down to 3-cm depth. The discontinuities in the predicted SNR difference correspond to small discontinuities in the

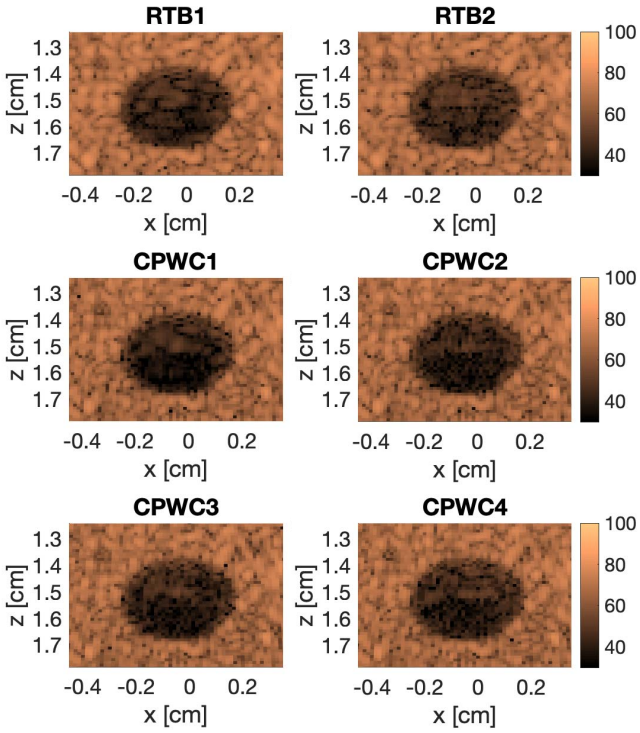

Fig. 8. Circular anechoic cyst imaged using different acquisition schemes.

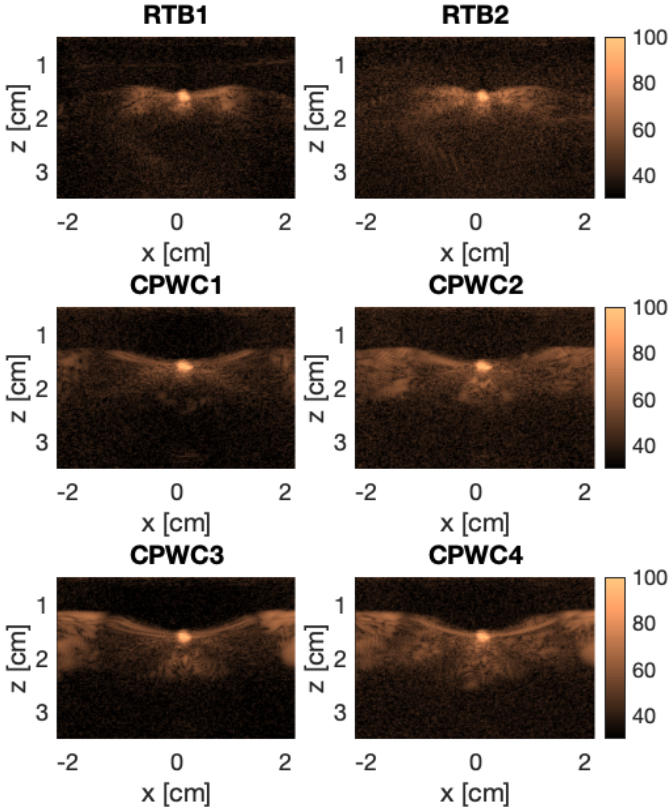

Fig. 9. Comparison of the PSF using the different acquisition schemes. Top: PSF using RTB1 and RTB2. Middle: CPWC1 and CPWC2 cases. Bottom: PSF employing CPWC3 and CPWC4.

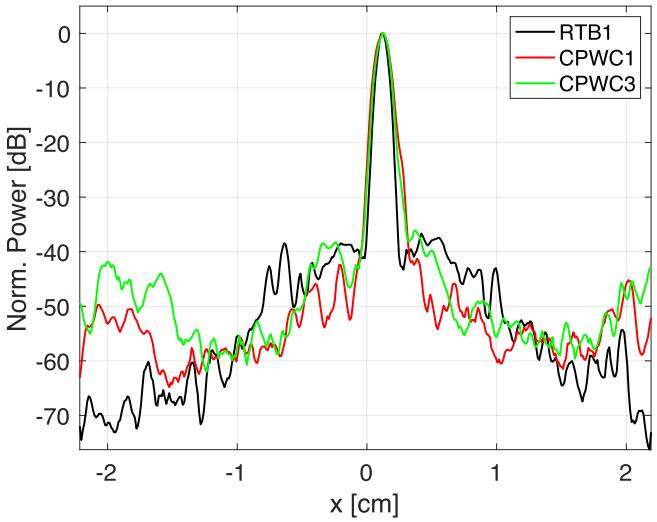

Fig. 10. Lateral profile of the PSF using RTB1, CPWC1, and CPWC3.

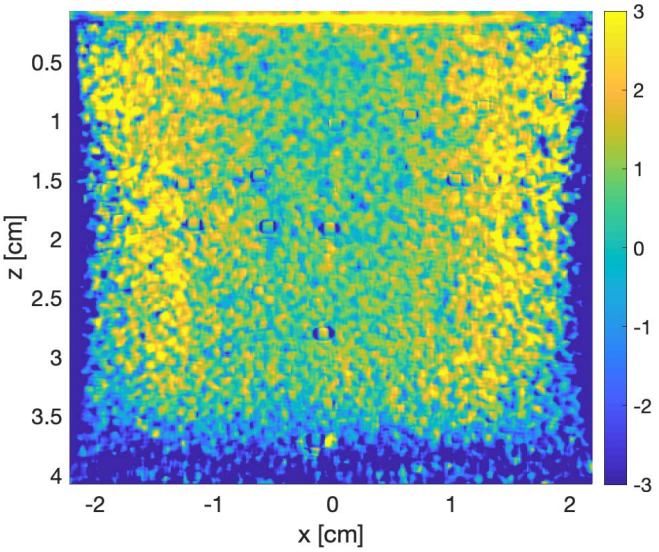

Fig. 11. SNR difference between the RTB1 and CPWC1 approaches using the stationary phantom. Values in the color bar are expressed in dB.

compounded signal as the contributions from additional transmissions are added to the signal.

Fig. 13 shows the predicted and measured SNR difference between RTB1 and CPWC1 as a function of maximum flow velocity. The measured values are based on the flow phantom recordings, and the summary statistics of the measured SNR difference is based on 213 points along the central axis of the tube. The median value of the SNR difference is given by the line in the middle of each box, whereas the bottom and top of each box correspond to the 25th and 75th percentiles, respectively. The range of the whiskers includes the remaining SNR differences in the sample. It may be observed that, as the velocity increases, the SNR difference between RTB1 and CPWC1 increases from approximately 1 dB in the stationary case (see also Fig. 12) to 6 dB at 15 cm/s.

Fig. 14 illustrates the predicted SNR difference between the different transmit sequences using a maximum flow velocity equal to 6 cm/s. RTB generally yields higher SNR than CPWC,

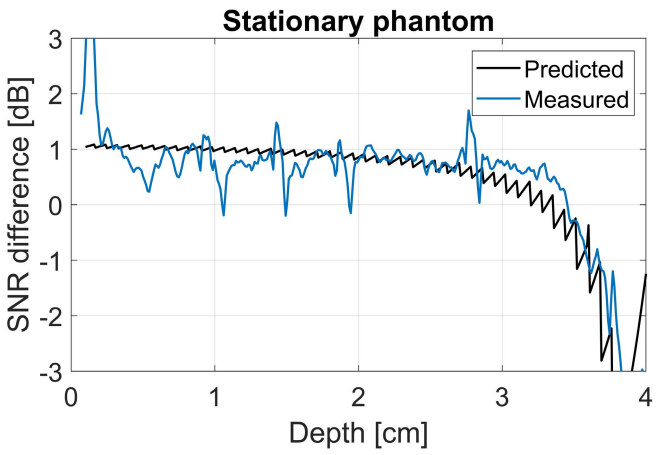

Fig. 12. Predicted and measured SNR difference between RTB1 and CPWC1 in the stationary phantom. The region of the stationary phantom used to generate the resulting SNR difference curve covered a lateral region from $x = -1.2$ to $x = 0.7$ cm.

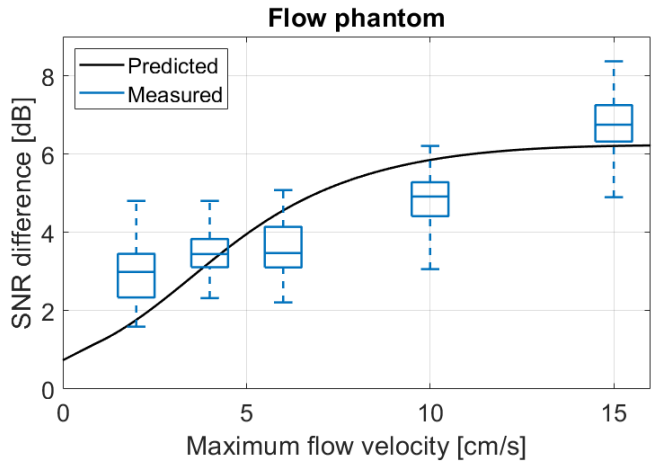

Fig. 13. Predicted and measured SNR difference between RTB1 and CPWC1 for moving scatterers.

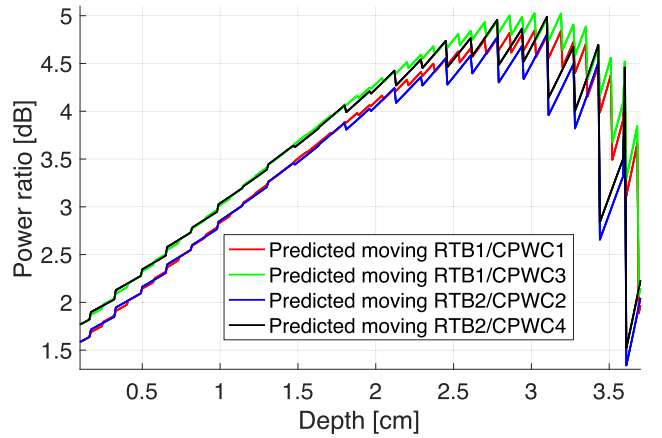

Fig. 14. Predicted SNR difference for different acquisition schemes using moving scatterers. In the red and green curves, RTB1 is compared with CPWC1 and CPWC3, respectively. The blue and black curves show the SNR difference when RTB2 is compared with CPWC2 and CPWC4. The maximum velocity is 6 cm/s.

with a peak difference at approximately 3-cm depth. When the lateral resolution of CPWC is increased (green and black curves), the SNR difference between RTB and CPWC also increases.

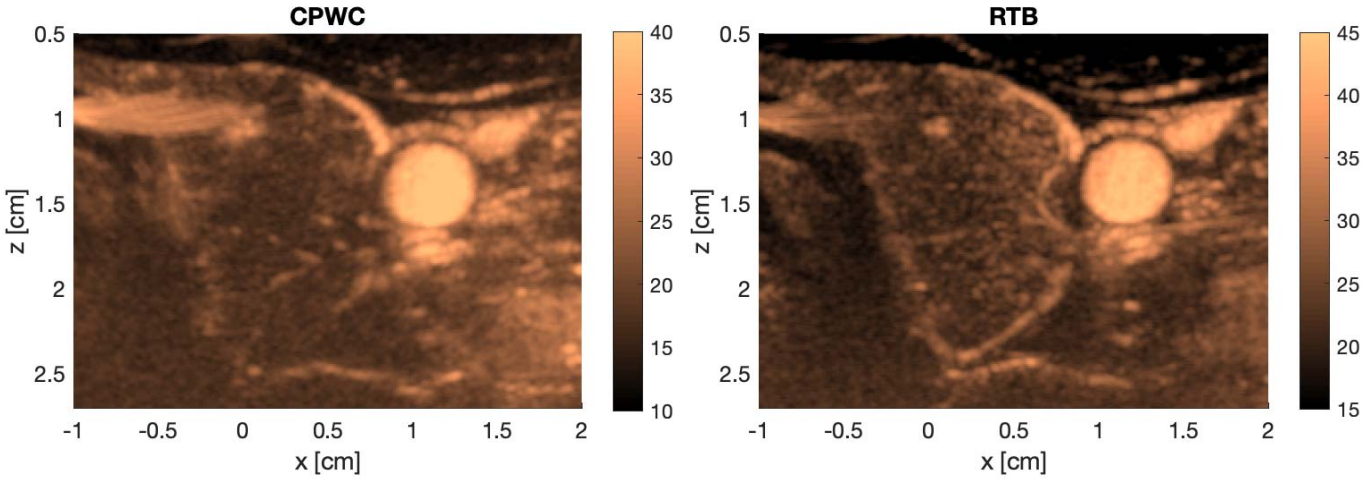

Fig. 15. Healthy thyroid: power Doppler images of the thyroid vessels and the carotid using CPWC1 and RTB1 sequences on the left and right figures, respectively.

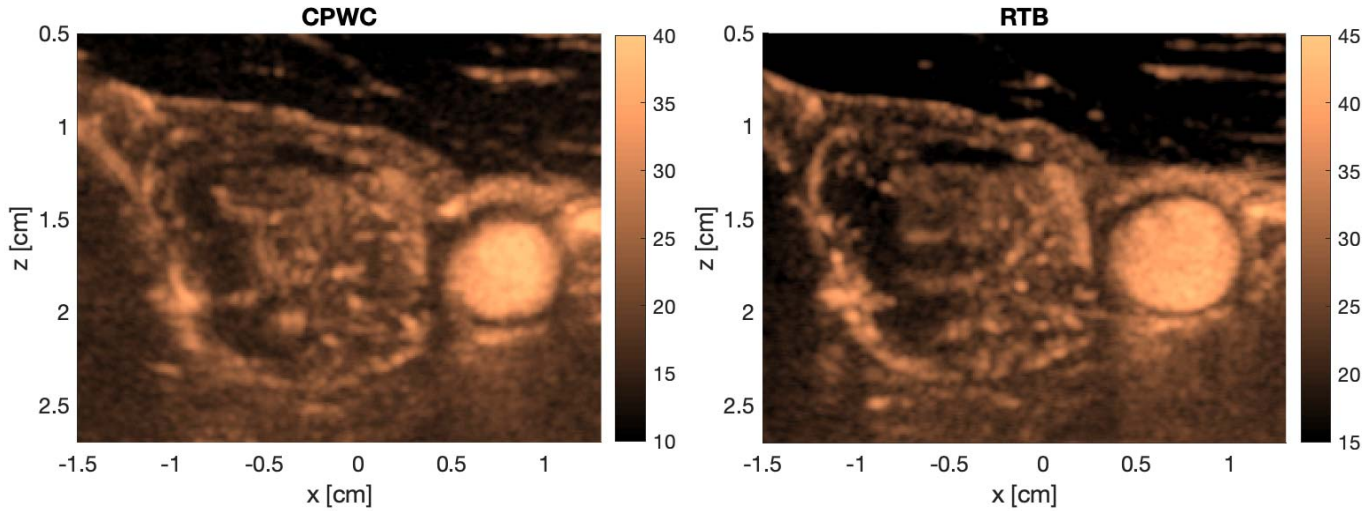

Fig. 16. Benign thyroid nodule: power Doppler images of increased thyroid vascularization using CPWC1 and RTB1 sequences on the left and right figures, respectively.

C. In Vivo Recordings

Figs. 15 and 16 display power Doppler images of thyroid vessels and parts of the common carotid artery using CPWC1 and RTB1. Fig. 16 shows increased vascularization due to the presence of a benign thyroid nodule.

Fig. 17 displays power Doppler images of blood vessels in the kidney of a healthy volunteer (see the videos in the Supplementary Material).

V. Discussion

In this study, the performance of CPWC and RTB were investigated for low-flow applications. The aim of this study was to compare the two techniques and investigate the advantages and disadvantages of each approach. Six transmit sequences were used: two RTB setups with 48 and 24 firings (RTB1 and RTB 2) and four CPWC sequences with the same number of transmissions as the RTB sequences and maximum steering angle 12° (CPWC1 and CPWC2) and 20° (CPWC3 and CPWC4). The resolution, contrast, and SNR differences between the RTB and CPWC sequences were measured using a stationary phantom, a flow phantom, and a thread phantom. A model was developed to predict the SNR difference using static and moving scatterers. The six transmit sequences were used to investigate artifacts in the image using both techniques. For the investigated sequences, the model predicted that RTB yields higher SNR, especially in presence of moving scatterers, for which the SNR difference reached 6 dB for a maximum velocity of 15 cm/s. The measured values of the SNR difference agreed well with predicted values, both in the case of stationary scatterers and for the flow phantom. We further demonstrated that the frame rate is limited either by undersampling artifacts in RTB or by grating lobes in CPWC.

Figs. 6 and 11 and Table III show that, for depths higher than 1 cm, resolution was higher using RTB1 than CPWC1. This is because $F_{\#tx}$ in RTB1 is equal to 1.4, whereas $F_{\#tx}$ in

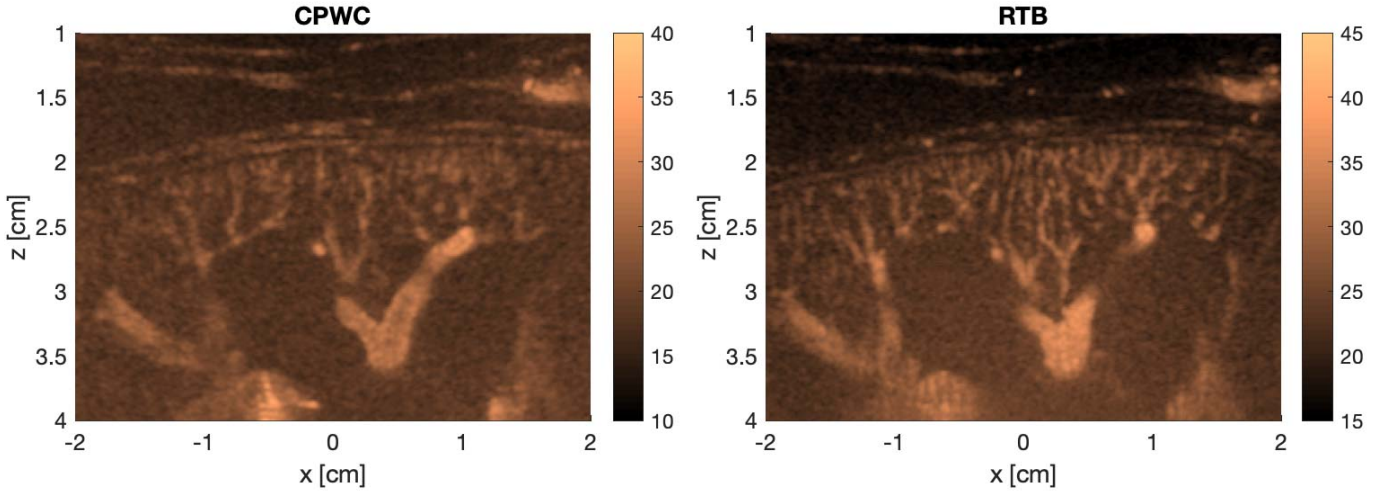

Fig. 17. Power Doppler images of the vessels in the kidney using CPWC1 and RTB1 sequences on the left and right figures, respectively.

CPWC1 is 2.4. To yield a similar resolution and frame rate in the CPWC approach as in the RTB approach, the maximum angle span in CPWC can be increased while maintaining the number of transmit angles. However, this introduces grating-lobe artifacts in the image, resulting in lower contrast. This is illustrated in Figs. 9 and 10, in which CPWC3 shows higher resolution compared with CPWC1, but, at the same time, grating lobes are more visible in the image. As can be seen in Fig. 9, lowering the number of plane waves while maintaining the maximum steering angle also leads to lower contrast, which corresponds well with the observation that grating lobes are stronger in CPWC2 and CPWC4 than CPWC1 and CPWC3, respectively. For both sequences, increased sidelobe leakage can be observed when decreasing the number of transmit beams.

In a stationary scenario, the predicted SNR difference presented in Fig. 12 is not affected by changes in the CPWC angle span. For shallow depths, all RTB beams and CPWC beams contribute to the backscattered echo strength, resulting in a given initial SNR difference. In our setup with the focal point at 4 cm, a decreasing number of RTB beams contributes to the signal as the depth increases, but, at the same time, the backscattered echo from each beam increases due to focusing. For a spatial region along the central axis of the transducer, the number of beams in CPWC that contribute to the signal is constant with depth independent of the angle span (disregarding element directionality), and they all contribute equally due to the lack of focusing. As a result, the SNR difference is more or less constant until a certain depth where the low number of overlapping RTB beams starts to affect the lateral sampling negatively.

In CPWC, all the elements of the transducer are activated at each transmission to reach the target depth with the same image width, whereas, in the designed RTB setups, 2/3 of the elements are activated for each emission. For a given transmit voltage, a smaller aperture yields less heating. For the given setup, the output power is the limiting factor; therefore, focusing the energy in the image field is beneficial to minimize energy loss. Fig. 11 illustrates the values of SNR difference between RTB1 and CPWC1 sequence using the stationary phantom. The RTB approach enables increased SNR, and higher SNR difference is present close to the edges compared with midimage. A possible explanation is that the number of overlapping beams in CPWC is lower on the sides.

It is possible that some of the differences observed in this study may be reduced by further optimizing the CPWC sequences. However, the abovementioned tradeoffs in image quality play an important role, for instance, in CPWC where increasing the maximum steering angle (while maintaining the number of firings) yields higher resolution but lower contrast. Note also that, for both RTB and CPWC, receive apodization may be applied to suppress sidelobes at the cost of reduced lateral resolution.

The main advantage of using RTB is that it is more robust in the presence of motion since fewer transmits are combined. For CPWC, for each point in the image, the contribution of energy from different transmissions will be fairly evenly distributed across all plane-wave transmissions. Image quality will then be affected by movement during the entire duration of the frame. For RTB, on the other hand, a lower number of transmissions contain the bulk of signal power in each pixel, implying less movement of each scatterer during the effective insonation time. As can be seen by comparing Figs. 12 and 14, predicted SNR difference using static and moving scatterers are comparable at depth 0.1 cm, where the number of compounded beams in RTB is almost equal to the number of compounded plane waves. At larger depths, RTB performs better as the number of compounded beams decreases. Note also that, for flow imaging, the SNR difference becomes slightly higher when a larger maximum angle is used. This is probably caused by a combination of lower transit time combined with an incoherent summation.

The frame rate of RTB sequences is limited compared with CPWC. For the latter, an image frame may be produced using only a few plane waves. However, this comes at the cost of stronger grating lobe artifacts. For the RTB approach,

transmitting fewer beams either results in reduced image width or degradation of image quality due to undersampling artifacts visible as vertical lines. In the right and bottom figure of Fig. 7, stripe artifacts are clearly visible at the bottom of the image, in the proximity of the focal depth. When increasing the number and, thus, the density of firings, these artifacts are significantly reduced.

The placement of the focal depth also plays an important role. In this study, the focal point was set at 4 cm. With this design choice, the region of interest was approximately halfway between the transducer and the focal depth with any stripe artifacts due to spatial undersampling being confined to the bottom of the image.

In vivo recordings using RTB and CPWC illustrate the feasibility of the designed setups for low-flow applications. Since the recordings were acquired in two different instants, a comparison in terms of SNR was not possible. However, comparable images were obtained, demonstrating that a valid low-flow imaging setup can be achieved based on focused pulses. The *in vivo* performance of RTB and CPWC for applications with higher blood velocities was not investigated in this work, but, as both acquisitions are using coherent compounding of successive firings, it is expected that the SNR gain for both modalities will be reduced for higher velocity flow.

VI. Conclusion

RTB was compared with CPWC for low-flow applications. Two RTB sequences were designed as potential improvements on reference CPWC sequences with the same frame rate. Analysis based on a signal model predicted higher SNR using the RTB sequences and increasing SNR difference for higher velocity flow. The predicted SNR difference reached 6 dB for a maximum velocity of 15 cm/s. Measurements were in good agreement with model predictions, with RTB achieving higher SNR than CPWC in phantom studies, as well as higher resolution and comparable contrast. *In vivo* feasibility was also shown, with similar images being produced from the two acquisitions. Results indicate that the RTB approach can be beneficial in a low-flow imaging setup.

References

[1] N. Ferrara, "Role of vascular endothelial growth factor in physiologic and pathologic angiogenesis: Therapeutic implications," *Seminars Oncol.*, vol. 29, no. 6, pp. 10–14, 2002.

[2] J. Gallo, M. Raska, E. Kriegova, and S. B. Goodman, "Inflammation and its resolution and the musculoskeletal system," *J. Orthopaedic Transl.*, vol. 10, pp. 52–67, Jul. 2017.

[3] G. Montaldo, M. Tanter, J. Bercoff, N. Benech, and M. Fink, "Coherent plane-wave compounding for very high frame rate ultrasonography and transient elastography," *IEEE Trans. Ultrason., Ferroelectr., Freq. Control*, vol. 56, no. 3, pp. 489–506, Mar. 2009.

[4] S. Bjærum, H. Torp, and K. Kristoffersen, "Clutter filters adapted to tissue motion in ultrasound color flow imaging," *IEEE Trans. Ultrason., Ferroelectr., Freq. Control*, vol. 49, no. 6, pp. 693–704, Jun. 2002.

[5] L. Lovstakken, S. Bjaerum, K. Kristoffersen, R. Haaverstad, and H. Torp, "Real-time adaptive clutter rejection filtering in color flow imaging using power method iterations," *IEEE Trans. Ultrason., Ferroelectr., Freq. Control*, vol. 53, no. 9, pp. 1597–1608, Sep. 2006.

[6] A. Yu and L. Lovstakken, "Eigen-based clutter filter design for ultrasound color flow imaging: A review," *IEEE Trans. Ultrason., Ferroelectr., Freq. Control*, vol. 57, no. 5, pp. 1096–1111, May 2010.

[7] C. Demené *et al.*, "Spatiotemporal clutter filtering of ultrafast ultrasound data highly increases Doppler and fUltrasound sensitivity," *IEEE Trans. Med. Imag.*, vol. 34, no. 11, pp. 2271–2285, Nov. 2015.

[8] P. Song, A. Manduca, J. D. Trzasko, and S. Chen, "Ultrasound small vessel imaging with block-wise adaptive local clutter filtering," *IEEE Trans. Med. Imag.*, vol. 36, no. 1, pp. 251–262, Jan. 2017.

[9] D. E. Kruse and K. W. Ferrara, "A new high resolution color flow system using an eigendecomposition-based adaptive filter for clutter rejection," *IEEE Trans. Ultrason., Ferroelectr., Freq. Control*, vol. 49, no. 10, pp. 1384–1399, Oct. 2002.

[10] I. K. Ekroll and J. Avdal, "Adaptive clutter filtering based on tissue vector velocities," in *Proc. IEEE Int. Ultrason. Symp. (IUS)*, Sep. 2017, pp. 1–4.

[11] V. Perrot *et al.*, "Spatial and temporal adaptive FIR clutter filtering," in *Proc. IEEE Int. Ultrason. Symp. (IUS)*, Oct. 2018, pp. 1–4.

[12] E. MacÉ, G. Montaldo, I. Cohen, M. Baulac, M. Fink, and M. Tanter, "Functional ultrasound imaging of the brain," *Nature Methods*, vol. 8, no. 8, pp. 662–664, 2011.

[13] E. Mace, G. Montaldo, B.-F. Osmanski, I. Cohen, M. Fink, and M. Tanter, "Functional ultrasound imaging of the brain: Theory and basic principles," *IEEE Trans. Ultrason., Ferroelectr., Freq. Control*, vol. 60, no. 3, pp. 492–506, Mar. 2013.

[14] I. K. Ekroll, M. M. Voormolen, O. K.-V. Standal, J. M. Rau, and L. Lovstakken, "Coherent compounding in Doppler imaging," *IEEE Trans. Ultrason., Ferroelectr., Freq. Control*, vol. 62, no. 9, pp. 1634–1643, Sep. 2015.

[15] R. T. Hoctor, D. J. Buckton, S. Jagannathan, M. P. Mienkina, and J. Jin, "Systems and methods for ultrasound retrospective transmit focus beamforming," U.S. Patent 9 366 753 B2, Feb. 19, 2015.

[16] B. Denarie *et al.*, "Coherent plane wave compounding for very high frame rate ultrasonography of rapidly moving targets," *IEEE Trans. Med. Imag.*, vol. 32, no. 7, pp. 1265–1276, Jul. 2013.

[17] A. Rodriguez-Molares, L. Lovstakken, B. Denarie, and H. Torp, "Busting the ghost in coherent plane-wave imaging," presented at the IEEE Int. Ultrason Symp., Taipei, Taiwan, Oct. 2015.

[18] N. Oddershede and J. Jensen, "Effects influencing focusing in synthetic aperture vector flow imaging," *IEEE Trans. Ultrason., Ferroelectr., Freq. Control*, vol. 54, no. 9, pp. 1811–1825, Sep. 2007.

[19] J. Jensen, M. B. Stuart, and J. A. Jensen, "Increased frame rate for plane wave imaging without loss of image quality," in *Proc. IEEE Int. Ultrason. Symp. (IUS)*, Oct. 2015, pp. 1–4.

[20] A. Rodriguez-Molares, J. Avdal, H. Torp, and L. Lovstakken, "Axial lobes in coherent plane-wave compounding," in *Proc. IEEE Int. Ultrason. Symp. (IUS)*, Sep. 2016, pp. 1–4.

[21] S. Nikolov and J. A. Jensen, "Virtual ultrasound sources in high-resolution ultrasound imaging," *Proc. SPIE*, vol. 4687, pp. 395–405, Apr. 2002.

[22] J. Baranger, B. Arnal, F. Perren, O. Baud, M. Tanter, and C. Demene, "Adaptive spatiotemporal SVD clutter filtering for ultrafast Doppler imaging using similarity of spatial singular vectors," *IEEE Trans. Med. Imag.*, vol. 37, no. 7, pp. 1574–1586, Jul. 2018.

Cristiana Golfetto was born in Genoa, Italy, in 1992. She received the M.Sc. degree in biomedical engineering from the University of Padua, Padua, Italy, in 2016. She is currently pursuing the Ph.D. degree in medical technology with the Norwegian University of Science and Technology, Trondheim, Norway.

During her master's studies, she spent one year as an exchange student at the Royal Institute of Technology, Stockholm, Sweden, where she worked on her thesis in the assessment of shear wave elastography acoustic output. Her research interest is in blood flow imaging.

Ingvild Kinn Ekroll (Member, IEEE) was born in Ålesund, Norway, in 1984. She received the M.Sc. degree in biophysics and the Ph.D. degree in medical technology from the Norwegian University of Science and Technology (NTNU), Trondheim, Norway, in 2009 and 2013, respectively.

She is currently a Researcher and an Associate Professor with the Department of Circulation and Medical Imaging, NTNU. Her research interests include tissue deformation and quantitative blood flow imaging techniques.

Hans Torp (Member, IEEE) was born in Sarpsborg, Norway, in 1953. He received the M.S. and Dr.Techn. degrees from the University of Trondheim, Trondheim, Norway, in 1978 and 1992, respectively.

Since 1983, he has been with the Department of Circulation and Medical Imaging, Faculty of Medicine, Norwegian University of Science and Technology, Trondheim, where he has been a full-time Professor since 1998. His research interests include stochastic signal/image processing with applications in ultrasonic imaging, Doppler, and color flow imaging.

Lasse Løvstakken (Member, IEEE) was born in Bergen, Norway, in 1976. He received the M.Sc. degree in engineering cybernetics and the Ph.D. degree in medical technology from the Norwegian University of Science and Technology, Trondheim, Norway, in 2002 and 2007, respectively.

He is currently a Professor with the Department of Circulation and Medical Imaging, Norwegian University of Science and Technology. His research interests include high-speed and real-time quantitative medical ultrasound, advanced image formation, visualization of blood and tissue dynamics, and machine learning.

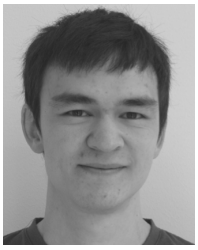

Jørgen Avdal (Member, IEEE) was born in Årdal, Norway, in 1984. He received the master's degree in industrial mathematics and the Ph.D. degree in medical technology from the Norwegian University of Science and Technology (NTNU), Trondheim, Norway, in 2009 and 2013, respectively.

He is currently an Associate Professor with the Department of Circulation and Medical Imaging, NTNU, where he is involved in ultrasound signal processing, blood flow imaging, and spectral Doppler applications.